

The metallicity evolution of blue compact dwarf galaxies from the intermediate redshift to the local Universe

Jianhui Lian¹, Ning Hu¹, Guanwen Fang², Chengyun Ye¹, Xu Kong¹

ljhhw@mail.ustc.edu.cn; xkong@ustc.edu.cn

ABSTRACT

We present oxygen abundance measurements for 74 blue compact dwarf (BCD) galaxies in the redshift range in $[0.2, 0.5]$ using the strong-line method. The spectra of these objects are taken using Hectospec on the Multiple Mirror Telescope (MMT). More than half of these BCDs had dust attenuation corrected using the Balmer decrement method. For comparison, we also selected a sample of 2023 local BCDs from the Sloan Digital Sky Survey (SDSS) database. Based on the local and intermediate- z BCD samples, we investigated the cosmic evolution of the metallicity, star-formation rate (SFR), and $D_n(4000)$ index. Compared with local BCDs, the intermediate- z BCDs had a systematically higher R23 ratio but similar O32 ratio. Interestingly, no significant deviation in the mass-metallicity (MZ) relation was found between the intermediate- z and local BCDs. Besides the metallicity, the intermediate- z BCDs also exhibited an SFR distribution that was consistent with local BCDs, suggesting a weak dependence on redshift. The intermediate- z BCDs seemed to be younger than the local BCDs with lower $D_n(4000)$ index values. The insignificant deviation in the mass-metallicity and mass-SFR relations between intermediate- z and local BCDs indicates that the relations between the global parameters of low-mass compact galaxies may be universal. These results from low mass compact galaxies could be used to place important observational constraints on galaxy formation and evolution models.

Subject headings: galaxies: dwarf – galaxies: evolution – galaxies: star formation – galaxies: fundamental parameters

¹CAS Key Laboratory for Research in Galaxies and Cosmology, Department of Astronomy, University of Science and Technology of China, Hefei, Anhui 230026, China

²Institute for Astronomy and History of Science and Technology, Dali University, Dali 671003, China

1. introduction

Metallicity is one of the most important parameters of galaxies and provides information on their past evolution. Many physical processes, such as star formation and gas inflow and outflow, involve the assembling of mass and the metal enrichment of a galaxy. A strong correlation between total mass (gas and stellar mass) and metallicity was found in the 1970s (Lequeux et al. 1979). Later on, Tremonti et al. (2004) confirmed this relation based on a sample of $\sim 50,000$ star forming galaxies at $z \sim 0.1$ from the Sloan Digital Sky Survey (SDSS; Abazajian et al. 2004). Galaxies with lower stellar mass tend to be less metal-enriched. They also found that the dispersion of the mass-metallicity (MZ) relation is lower than that of luminosity-metallicity relation and concluded that the former is more fundamental. With deep spectroscopic surveying of distant galaxies, it is possible to investigate the MZ relation in the early universe. Recently, the MZ relation at intermediate and high redshift has been extensively explored (Savaglio et al. 2005; Erb et al. 2006; Maiolino et al. 2008; Zahid et al. 2011; Yuan et al. 2013). When the MZ relations at different redshifts are compared, galaxies at higher redshift tend to be more metal-poor at a fixed stellar mass. This trend was often regarded as the cosmic evolution of the MZ relation (Maiolino et al. 2008). The evolution of the MZ relation was also found when comparing the analogs of high redshift galaxies with local star-forming galaxies (Hoopes et al. 2007; Lian et al. 2015). However, such a comparison may be significantly affected by the different sample selection criteria and different methods for metallicity and stellar mass determination (Izotov et al. 2015).

The MZ relation is an important probe for the balance between gaseous inflows, outflows, and star formation. One possible explanation for the MZ relation is supernova-driven winds, which could remove the metal-enriched gas and are more effective in low-mass galaxies with a shallow gravitational potential. It is also suggested by many studies that outflows are prevalent in low-mass galaxies (Izotov et al. 2006a; Martin et al. 2012). However, the properties of these gaseous flows are poorly constrained and the physical driver of the MZ relation is still under debate. A better understanding of the MZ relation at low mass are important to fully understand the MZ relation and how galaxies evolve at the early stage. There are many studies of the local MZ relation (or luminosity-metallicity relation) of low-mass galaxies (Lee et al. 2006; Zhao et al. 2010; Berg et al. 2012). However, outside the local universe, the MZ relation at stellar masses below $10^9 M_\odot$ is not yet well established.

Blue compact dwarf (BCD) galaxies are faint ($M_B > -17$ mag) objects and have distinctive compact morphology. Strong emission lines in optical spectra indicate that they are undergoing active star formation (Sargent & Searle 1970; Kunth & Östlin 2000; Kong & Cheng 2002). According to hierarchical galaxy-formation scenarios, dwarf galaxies are part of the building blocks for massive galaxies in the early universe. The gas consumption

timescale of BCDs, given the current SFR, is much shorter than the age of the universe (Kong 2004). In this work, we consistently select BCDs at the intermediate- z and local universe and investigated the possible cosmic evolution of the MZ relation at the low-mass end.

This paper is organized as follows. In Section 2, we describe the selection of BCDs at different redshifts and the spectroscopic observation of BCDs at intermediate redshift. The measurements for emission lines and physical properties such as stellar mass, SFR, $D_n(4000)$ index and metallicities are described in Section 3. We then provide the MZ relation of BCDs at different redshifts using the same metallicity determination method in Section 4. In this part, we also investigate the possible evolution of the SFR and $D_n(4000)$ index. Finally, we present a summary in Section 5. Throughout this paper, we adopt the cosmological parameters $H_0 = 70 \text{ kms}^{-1}\text{Mpc}^{-1}$, $\Omega_\Lambda = 0.73$ and $\Omega_m = 0.27$.

2. Sample selection and observation

2.1. BCDs at $z \sim 0.03$

There are many definitions of BCD in the literature (Thuan & Martin 1981; Kong & Cheng 2002; Gil de Paz et al. 2003). Generally, BCDs are characterized by their blue color, compact morphology, and low luminosity or stellar mass. Gil de Paz et al. (2003) proposed quantified classification criteria to select BCDs as follows: 1) blue color with $B - R < 1$; 2) compact with peak surface brightness in the B band $\mu_B < 22 \text{ mag arcsec}^{-2}$; and 3) faint with $M_K < -21 \text{ mag}$. Later on, Sánchez Almeida et al. (2008) used a set of similar criteria based on SDSS filters (see Table 3 in Sánchez Almeida et al. 2008). According to the definition of BCD in Sánchez Almeida et al. (2008), we selected galaxies from SDSS DR12 (Alam et al. 2015) that satisfied the following criteria as our BCD sample in the local universe: 1) blue color with $\mu_g - \mu_r < 0.43 \text{ mag arcsec}^{-2}$, where μ_g is the mean surface brightness within r_{50} in the g band; 2) compact with $\mu_g < 21.83 - 0.47(\mu_g - \mu_r)$; 3) dwarf with stellar mass $M_* < 10^9 M_\odot$; 4) stellar mass error $\Delta m < 0.25 \text{ dex}$; 5) redshift $z < 0.05$; 6) signal-to-noise ratio (SNR) of $[\text{O II}]\lambda 3727$, $\text{H}\beta$, $[\text{O III}]\lambda\lambda 4959, 5007$ emission line above 5. All of the measurements were taken from the MPA-JHU catalog¹ (Kauffmann et al. 2003; Brinchmann et al. 2004). Since the error of the stellar mass is not directly given in the MPA-JHU catalog, we estimated the error by calculating half of the difference between the 84th percentile and the 16th percentile probability distribution of the stellar mass (i.e. the

¹<http://skyserver.sdss.org/dr12/en/help/browser/browser.aspx>

lgm_tot_p84 and lgm_tot_p16 index) in the MPA-JHU catalog. Contamination of the HII regions in nearby galaxies was excluded by visually inspecting the SDSS image. Finally, 2023 galaxies were selected as our local BCD sample with a median redshift of 0.03 and a median equivalent width (EW) $H\beta$ of 14.9 Å. Among them, 262 BCDs had [O III]λ4363 line detected at the 5σ level.

2.2. BCDs in the COSMOS field

To study low-mass galaxies outside the local universe, we selected a BCD sample at intermediate redshift in the Cosmic Evolution Survey (COSMOS) deep field and then performed follow-up spectroscopic observation using Hectospec on the Multiple Mirror Telescope (MMT). We selected the BCD sample from a public K_s selected catalog of the COSMOS field (Muzzin et al. 2013). COSMOS is a Hubble Space Telescope (HST) Treasury Project to survey a two-square-degree equatorial field with comprehensive observations from radio to X-ray. We searched for BCDs in a one-degree diameter circle centered at RA = 150.1152, Dec = 2.3420 (J2000). Only galaxies at redshift lower than 0.7 were selected because the [O III]λ5007 line at higher redshift will be redshifted beyond the wavelength coverage of the Hectospec/MMT. For the dwarf criteria, we used the stellar mass M_* , which could be accurately measured based on 27 broad- and intermediate-band filters. To reliably estimate the peak surface brightness, high-resolution imaging is needed. Since only one HST band at 0.814 μm is available, we obtained an image cut for each dwarf galaxy and then calculated the peak surface brightness in the $F814W$ band using SExtractor (Bertin & Arnouts 1996). A correction factor of $(1+z)^4$ was applied to the surface brightness to account for the redshift dimming effect. To roughly cover the restframe $U - B$ color of the intermediate-redshift objects, we use the observed $u - i$ color based on the SDSS filter system. The distribution of the $u - i$ color of dwarf galaxies in the catalog has a Gaussian profile with a median of 1.3, rather than the bimodal distribution found for massive galaxies (Baldry et al. 2004). We decided to select the bluer half dwarf galaxies to exclude possible contamination by red early-type dwarf galaxies. According to the Mass-Excitation diagram (Juneau et al. 2011), the AGN fraction at $M_* < 10^9 M_\odot$ is negligible. Therefore, we did not exclude AGN contamination from the BCD sample. The final criteria for BCDs in the COSMOS field were: 1) $u - i < 1.3$; 2) $\mu_{F814W, \text{peak}} < 22 \text{ mag arcsec}^{-2}$; 3) $M_* < 10^9 M_\odot$; 4) $z < 0.7$. In total, ~ 1400 objects were selected as a parent sample of BCD. We then ran the XFITFIBS program which was developed for Hectospec to allocate the fibers to the objects. Every pair of objects should be separated by at least $22''$ to avoid fiber collision. In the end, 180 BCDs with a median redshift of 0.39 and 28 sky background regions were assigned to a fiber.

The observations of these BCDs using the Hectospec/MMT were carried out in 2015 February. Hectospec is a moderate-resolution, multi-object spectrograph, fed by 300 fibers. Each fiber has a diameter of $1.5''$ (corresponding to 5 kpc at $z = 0.2$) and covers most of the light of BCDs at intermediate redshift. The field of view is a circle with a diameter of 1° . We chose the 270-line grating with a resolution of 1.2 \AA per pixel to achieve wider wavelength coverage from 3650 \AA to 9200 \AA and a wavelength resolution of $\sim 6 \text{ \AA}$. Figure 1 shows the restframe spectra smoothed using a boxcar of five pixels for the first four COSMOS BCDs as listed in Table 1. The fiber spectra were reduced using the HSRED reduction pipeline. The data were flux calibrated using the observation of one standard star, PG-1545+035, taken 1 week before the science observation. Sky subtraction was achieved by averaging the spectra of sky regions from the same exposure. With an exposure time of 4 hours, 141 objects had $[\text{O III}]\lambda\lambda 4959, 5007$ double lines detected at a level above 3σ . Figure 2 shows the comparison between the spectroscopic redshift from this observation and the photometric redshift in the catalog of Muzzin et al. (2013). There are eight objects that have spectroscopic redshift from the zCOSMOS survey (Lilly et al. 2009) and they are marked as filled circles in Figure 2. It can be seen that the photometric redshifts are roughly consistent with the spectroscopic redshifts with an offset of -0.007 ± 0.112 dex.

3. Emission-line Measurements

Emission-line measurements of the SDSS BCD sample were taken from the MPA-JHU catalog. For BCDs in the COSMOS field, after subtracting the spectra continuum, we obtained line fluxes by fitting Gaussian profiles to each line using the MPFIT routine (Markwardt 2009). Since most of the COSMOS BCDs are faint, their spectra continua are marginally detected. To subtract the spectra continuum and estimate the significance of emission lines, we followed the method in Ly et al. (2014). Firstly, for each line, we picked a 200 \AA -wide spectrum, excluding regions affected by sky lines and nebular emissions. The spectra continuum is assumed to be the median of this spectrum. We then computed the SNR by dividing the line flux by:

$$\text{Noise} = \sigma \times l \times \sqrt{N_{\text{pixel}}}, \quad (1)$$

, where σ is the standard deviation of the 200 \AA -wide spectra, l is the spectral resolution and $N_{\text{pixel}} = 5\sigma_{\text{G}}/l$ (also see equation 3 in Ly et al. (2014)). σ_{G} is the Gaussian width of the emission line.

To derive the metallicity using the R23 method ($R23 = \log([\text{O II}]\lambda 3727 + [\text{O III}]\lambda\lambda 4959, 5007)/\text{H}\beta$), we selected a subsample of 74 COSMOS BCDs whose strongest emission lines had an SNR

above 3σ and with a redshift in the range $[0.2, 0.5]$ as in our COSMOS BCD sample. Since the diameter of the MMT is 2.6 times larger than that of the SDSS and the exposure time is 5.3 times longer, the SNR criteria of the SDSS BCDs were actually higher than for the COSMOS BCDs by a factor of 10, which is roughly proportional to $1/z$. Therefore, these two BCD samples should be comparable with consistent emission-line selection criteria. All of the line fluxes of the COSMOS and SDSS BCDs were corrected for galactic foreground extinction. Since the spectra continua are marginally detected, we were not able to accurately determine the Balmer absorption. Zahid et al. (2011) estimated the Balmer absorption, which is $\sim 1 \text{ \AA}$ in EW, for star-forming galaxies at $z \sim 0.8$. According to their result, we applied a correction of 1 \AA in EW for the Balmer absorption to our Balmer emission-line measurements. It should be noted that such correction did not significantly affect our results, as it is small compared to the $\text{EW}(\text{H}\beta)$ of COSMOS BCDs, with a median value of 30.2 \AA .

Since the R23 indicator is sensitive to dust attenuation, it is important to reliably determine the intrinsic extinction. In this work, we used the Balmer decrement method to determine the dust attenuation assuming a Calzetti extinction law (Calzetti et al. 2000). Since the spectra are affected by contamination of second-order light at wavelengths longer than $\sim 8200 \text{ \AA}$, the $\text{H}\alpha$ line can not be detected or reliably flux calibrated for BCDs at $z > 0.25$. For consistency, we used the $\text{H}\beta/\text{H}\gamma$ ratio to estimate the dust attenuation assuming an intrinsic ratio of 2.14. However, of the COSMOS BCD samples, only 38 BCDs had an SNR of the $\text{H}\gamma$ line above 3σ . For the rest of the 36 COSMOS BCDs, we used the color excess $E(B - V)$ from SED fitting to roughly estimate the intrinsic extinction. It should be noted that the nebular extinction was higher than the stellar extinction. Although the exact relation between the nebular and the stellar extinction is under debate, we adopted a factor of 2.3 to transfer the stellar extinction from the SED fit to the dust extinction of the emission lines (Calzetti et al. 2000; Cresci et al. 2012). In the rest of this paper, we will distinguish between the COSMOS BCDs using these two extinction determination methods. The extinction-corrected emission-line fluxes are listed in Table 1. We do not provide an estimate of the uncertainties of the extinction from the SED fit which was strongly dependent upon the other SED fitting parameters. Of the COSMOS BCDs with dust extinction corrected using the Balmer decrement method, two-thirds exhibited negligible dust extinction ($A_V = 0$). In these cases, the uncertainties of the dust extinction can not be precisely determined. Therefore, we did not propagate the uncertainties of the dust extinction to that of the extinction-corrected emission-line fluxes.

The extinction $E(B-V)$ would be negative for galaxies with an $\text{H}\beta/\text{H}\gamma$ ratio of less than 2.14. In these cases, we manually set the extinction to 0 since the dust extinction seemed to be negligible, which was indicated by the relatively low $\text{H}\beta/\text{H}\gamma$ ratio. Figure 3 shows the R23 and O32 ($\text{O32} = \log([\text{O III}]\lambda 5007 / [\text{O II}]\lambda 3727)$) ratios versus the stellar mass. The grey

dots represent the SDSS BCDs and the red circles are the COSMOS BCDs. The filled circles are the BCDs with dust attenuation corrected using the Balmer decrement method. The R23 ratio of the COSMOS BCDs seems to be systematically higher than that of the SDSS BCDs at $M_* > 10^8 M_\odot$, while the O32 ratios of the two BCD samples are rather similar.

4. Physical properties Determination

The total stellar mass of the SDSS BCD sample was taken from the MPA-JHU catalog where a Kroupa IMF (Kroupa 2001) was assumed. The MPA-JHU team obtained the stellar mass based on Bruzual & Charlot (2003) (hereafter BC03) population synthesis model and assuming an exponentially-declining star formation history. The stellar mass of the COSMOS BCD sample was determined by fitting the stellar population templates to 27 emission-line-corrected broad- and intermediate-band filters using the Fitting and Assessment of Synthetic Templates (FAST; Kriek et al. 2009) code. The original photometric were taken from the photometry catalog of Muzzin et al. (2013). Since BCDs typically have high emission-line EW, we needed to correct the broad- and intermediate- band photometry for the contribution from emission lines. For each galaxy, we generated a redshifted spectrum with emission-lines and zero continua. We then convolved these spectra with the 27 filter bandpasses to determine the flux excesses, and then removed the excesses from the original photometry. For the objects without reliable $H\alpha$ detection, we estimated the contribution from $H\alpha$ based on $H\beta$ measurements, assuming an $H\alpha/H\beta$ ratio of 2.86. To allow a direct comparison with local BCDs, we chose the BC03 population synthesis model and adopted an exponentially-declining star-formation history to perform the SED fit. However, there is no Kroupa IMF-based BC03 model available in the FAST default settings. Therefore, we adopted a Chabrier IMF (Chabrier 2003) and then applied a correction factor of 1.06 to transfer to the Kroupa IMF based stellar mass.

The SFR of the BCDs was determined using the relation between the extinction-corrected $H\alpha$ luminosity and the SFR in Hao et al. (2011). Since most COSMOS BCDs have no $H\alpha$ detection, $H\beta$ luminosity was used instead, assuming the intrinsic ratio of $H\alpha/H\beta$ to be 2.86. In the burst scenario, $H\alpha$ and $H\beta$ EWs strongly decline with the starburst age (Leitherer et al. 1999; Izotov et al. 2015). Therefore, to perform a fair comparison, we corrected the SFR to the initial stage of burst according to equation (5) in Izotov et al. (2015). However, it should be noted that the correction will be overestimated when there are old populations present in the galaxy. The overestimation will be stronger for galaxies with lower $EW(H\beta)$. The SFR measurements of SDSS BCDs were corrected for the aperture effect, which was estimated using the difference between the model and the fiber magnitude

at the u band as $10^{(u_{\text{fiber}} - u_{\text{total}})/2.5}$. The aperture corrections are small, with a median value of 2.8. We did not apply aperture corrections for the COSMOS BCDs because the fiber coverage could be higher than the local BCDs by an order of magnitude and the corrections must be negligible. We calculated the 4000 Å break [i.e. $D_n(4000)$ index] based on the definition of Balogh et al. (1999). Since the spectra continuum are marginally detected, 42 of the COSMOS BCDs have reliable measurements of $D_n(4000)$ index with 3σ uncertainty less than 0.11.

There are many methods for obtaining the metallicity of an emission-line galaxy. One of the most direct is the so-called ‘ T_e -method’, which utilizes the anticorrelation between the metallicity and the electron temperature T_e . The electron temperature can be derived from the ratio of the auroral to the nebular emission lines. However, the auroral lines, such as [O III]λ4363, are always very weak. Therefore, many empirical and theoretical calibrations are proposed. Although these calibrations are all based on strong-line ratios, the difference could be as large as 0.7 dex (Shi et al. 2005; Kewley & Ellison 2008). The origin of this difference is still not fully understood.

In this work, we obtained the metallicity using the relation between the metallicity and the R23 ratio and the O32 ratio. Since there are two metallicity solutions for one R23 value, extra information is needed to discriminate the upper or lower metallicity solution. The diagnostics for distinction should be sensitive to metallicity. The most widely-used is the ratio of [N II]λ6584/Hα or [N II]λ6584/[O II]λ3727 (Kewley & Ellison 2008). However, the [N II]λ6584 is redshifted to the infrared at intermediate redshift and sky lines could strongly contaminate this weak emission line. Therefore, other methods without the information of [N II]λ6584 are needed to break the R23 degeneracy. Other parameters, such as the O32 line ratio and stellar mass, are proposed to break the R23 degeneracy (Maiolino et al. 2008; Henry et al. 2013). Maiolino et al. (2008) (hereafter M08) first calibrated the R23- and O32-metallicity relations by combining the T_e method and photoionization models. Then, metallicities in their work were derived by minimizing the difference from the expectations of the R23 and O32 measurements simultaneously. Henry et al. (2013) determined metallicities using the R23 calibration from Kobulnicky & Kewley (2004) but utilized stellar mass to break the R23 degeneracy. For a subsample of 262 local BCDs which have [O III]λ4363 detected, we compared the metallicities determined using these two methods to that derived from the direct T_e method (Izotov et al. 2006b). The M08 method shows a stronger correlation with the T_e method than the method used in Henry et al. (2013). We also derived the metallicities for local BCDs using N2 method (Pettini & Pagel 2004), $12 + \log(\text{O}/\text{H}) = 8.9 + 0.57 * \log([\text{N II}]/\text{H}\alpha)$, which is monotonic and insensitive to dust attenuation. Metallicities derived using the M08 method also show a stronger correlation with that derived using the N2 method. In total, we consider the M08 method to be more robust

than the KK04 calibration with stellar mass for breaking the R23 degeneracy. Therefore, in this work, we adopted the method from Maiolino et al. (2008) to derive the metallicity of BCDs.

We repeated the metallicity determination process 1000 times while the emission-line fluxes varied based on their uncertainties. The median value of the 1000 measurements was the final metallicity and the median of the absolute deviation from the final metallicity was the error of metallicity. The obtained measurements of all the parameters mentioned above are listed in Table 2.

5. Results

5.1. Mass-metallicity relation

The MZ relations at intermediate and high redshift have been extensively explored. However, most of the work has focused on massive star-forming galaxies, which can be reached at high redshift. Recently, Henry et al. (2013) were the first to derive the low-mass, intermediate- z MZ relation based on 26 emission-line galaxies at $z \sim 0.6 - 0.7$. Most of the galaxies in their sample had a stellar mass higher than $\sim 10^{8.4} M_{\odot}$. They obtained metallicities using the R23 calibration from Kobulnicky & Kewley (2004). Based on the MZ relation, they utilized stellar mass to chose the appropriate branch of the R23 solution. They found that the metallicity is typically lower than that at $z \sim 0.1$ by about 0.12 dex at a fixed mass. However, the dust extinction in their work was estimated using SED fitting, which may suffer large uncertainties.

In this work, we aimed to study the intermediate- z MZ relation at the lower stellar mass end with a much larger and more complete sample. Figure 4 shows the MZ relation of the intermediate- z COSMOS and local SDSS BCDs. The gray dots represent the SDSS BCDs. The red filled circles are the COSMOS BCDs with dust extinction corrected using the Balmer decrement method, while the empty circles represent the correction from SED fitting. The dashed line is the best-fitting MZ relation to the local BCDs as:

$$12 + \log(\text{O}/\text{H}) = 4.55(\pm 0.10) + 0.46(\pm 0.01) \times M_{*}. \quad (2)$$

All stellar mass values were calibrated to be consistent with the Kroupa IMF and the metallicities with calibration from Maiolino et al. (2008).

It is interesting that the COSMOS BCDs have metallicities that are fairly consistent with those of the local BCDs with a slight deviation of -0.05 ± 0.16 dex. Although the

intermediate- z BCDs have R23 ratios systematically higher than the local BCDs, the difference in metallicity is not significant. This is mainly because intermediate- z BCDs have intermediate metallicity where the R23 ratio is not a monotonic function of the metallicity. Meanwhile, the intermediate- z BCDs have O32 ratios similar to local BCDs which could reduce the difference in the metallicities caused by different R23 ratios. The consistent MZ relation between the intermediate- z and local BCDs suggests that the cosmic evolution of metallicity is not significant in low-mass galaxies from redshift $z \sim 0.3$ to ~ 0.03 . This is not consistent with the result found by Henry et al. (2013). We consider that the different method used for metallicity determination is the main reason for this inconsistency. It should be noted that our sample was about three times larger and the method of metallicity determination adopted in the work was more consistent with other metallicity calibrations, such as the T_e method. However, our metallicity measurements derived by the M08 method still suffered large uncertainties. Information on [NII] is important to derive metallicities with multiple calibrations to confirm or deny our result. These calibrations are monotonic with metallicity and do not have the two-solution problem.

5.2. Evolution of SFR and $D_n(4000)$

Besides metallicity, we also obtained the SFR and $D_n(4000)$ of BCDs. Figure 5 shows BCDs in the mass-SFR and mass- $D_n(4000)$ diagram. The dashed lines represent the best-fitting relation to the SDSS BCDs. It can be seen that intermediate- z BCDs exhibit a consistent mass-SFR (main sequence) relation with local BCDs. The median deviation of the COSMOS BCDs from the best-fitting line is 0.05 dex which is not significant compared with the dispersion in the main sequence relation of 0.32 dex. In contrast, the offset between the two BCD samples in the mass- $D_n(4000)$ relation seems to be larger, being two times higher than the scatter.

According to the downsizing evolution scenario, low-mass galaxies may experience star formation that decreases less in the recent universe than in massive galaxies. The insignificant deviation in SFR between the intermediate- z and local BCDs may be due to the large scatter in the main sequence relation and narrow redshift range. However, Izotov et al. (2015) investigated aperture-corrected compact galaxy global parameters, including stellar mass, gas-phase oxygen abundance, and SFR, in a wide range of redshift up to 3 and found weak redshift evolution. This is consistent with our results that no significant deviation in MZ and main sequence relation is found between intermediate- z and local BCDs. The lower $D_n(4000)$ of the intermediate- z BCDs, indicating a younger stellar population, is reasonable, since they were located in the universe ~ 3 Gyrs earlier than the local BCDs.

6. Summary

In this work, we have investigated the cosmic evolution of the metallicity, SFR, and $D_n(4000)$ of low-mass compact star-forming galaxies from intermediate redshift to the local universe. We selected a local BCD sample from the SDSS database and an intermediate- z BCD sample from the COSMOS deep field. Using Hectospec on the MMT, we obtained optical spectra for 180 COSMOS BCDs. Among them, 74 objects had reliable detection of strong emission lines, which allows metallicity determination based on the strong-line method. Of the COSMOS BCD sample, more than half had reliable $H\gamma$ detection and had dust extinction corrected using the Balmer decrement method. The main results and conclusions were as follows.

- Intermediate- z BCDs have R23 ratios systematically higher than local BCDs, while no significant difference was found with the O32 ratio.
- We obtained oxygen abundance measurements for 74 COSMOS BCDs based on the strong-line method from Maiolino et al. (2008). Interestingly, the MZ relation of BCDs at the intermediate redshift is fairly consistent with that of the local BCDs. with a slight deviation of -0.05 ± 0.16 dex.
- In addition to metallicity, no significant deviation in the mass-SFR relation was found between the intermediate- z and local BCDs. On the other hand, the intermediate- z BCDs seemed to be younger than the local BCDs, with lower $D_n(4000)$ index values. However, the deviation in $D_n(4000)$ index values is not statistically significant which may be due to the narrow redshift range.

The insignificant deviation in MZ and mass-SFR relation between intermediate- z and local BCDs indicates that these relations between the global parameters of low-mass compact galaxies may be universal. These results of low-mass compact galaxies may provide important observational constraints onto the galaxy-formation and evolution model.

Acknowledgments

We are grateful to referee’s insightful suggestions and comments. We thank Yang, C. W. for his help in emission line measurements, Caldwell, N. for his help in preparing observation and people in SAO Telescope Data Center for their help in data reduction. This research uses data obtained through the Telescope Access Program (TAP), which has been funded by the National Astronomical Observatories of China, the Chinese Academy of Sciences (the

Strategic Priority Research Program ‘The Emergence of Cosmological Structures’ Grant No. XDB09000000), and the Special Fund for Astronomy from the Ministry of Finance. Hectospec observations reported here were obtained at the MMT Observatory, a joint facility of the University of Arizona and the Smithsonian Institution. This work is supported by the Strategic Priority Research Program ‘The Emergence of Cosmological Structures’ of the Chinese Academy of Sciences (No. XDB09000000), the Chinese National 973 Fundamental Science Programs (973 program) (2015CB857004), the National Natural Science Foundation of China (NSFC, Nos. 11225315, 1320101002, 11433005, 11421303, and 11303002), the Specialized Research Fund for the Doctoral Program of Higher Education (SRFDP, No. 20123402110037), the Yunnan Applied Basic Research Projects (2014FB155), and the Open Research Program of Key Laboratory for Research in Galaxies and Cosmology, CAS.

REFERENCES

- Abazajian, K. et al. 2004, *AJ*, 128, 502
- Alam, S., Albareti, F. D., Allende Prieto, C., et al. 2015, arXiv:1501.00963
- Baldry, I. K., Glazebrook, K., Brinkmann, J., et al. 2004, *ApJ*, 600, 681
- Balogh, M. L., Morris, S. L., Yee, H. K. C., Carlberg, R. G., & Ellingson, E. 1999, *ApJ*, 527, 54
- Berg, D. A., Skillman, E. D., Marble, A. R., et al. 2012, *ApJ*, 754, 98
- Bertin, E., & Arnouts, S. 1996, *A&As*, 117, 393
- Brinchmann, J., Charlot, S., White, S. D. M., Tremonti C., Kauffmann G., Heckman T., Brinkmann J., 2004, *MNRAS*, 351, 1151
- Bruzual, G., & Charlot, S. 2003, *MNRAS*, 344, 1000 (BC03)
- Calzetti, D., Armus, L., Bohlin, R. C., Kinney A. L., Koornneef J., Storchi-Bergmann T., 2000, *ApJ*, 533, 682
- Chabrier, G. 2003, *PASP*, 115, 763
- Cresci, G., Mannucci, F., Sommariva, V., et al. 2012, *MNRAS*, 421, 262
- Erb, D. K., Steidel, C. C., Shapley, A. E., Pettini M., Reddy N. A., Adelberger K. L., 2006, *ApJ*, 646, 107

- Gil de Paz, A., Madore, B. F., & Pevunova, O. 2003, *ApJS*, 147, 29
- Hao, C.-N., Kennicutt, R. C., Johnson, B. D., et al. 2011, *ApJ*, 741, 124
- Henry, A., Martin, C. L., Finlator, K., & Dressler, A. 2013, *ApJ*, 769, 148
- Hoopes, C. G., Heckman, T. M., Salim, S., et al. 2007, *ApJS*, 173, 441
- Izotov, Y. I., Schaerer, D., Blecha, A., et al. 2006, *A&A*, 459, 71
- Izotov, Y. I., Stasińska, G., Meynet, G., Guseva, N. G., & Thuan, T. X. 2006, *A&A*, 448, 955
- Izotov, Y. I., Guseva, N. G., Fricke, K. J., & Henkel, C. 2015, *MNRAS*, 451, 2251
- Juneau, S., Dickinson, M., Alexander, D. M., & Salim, S. 2011, *ApJ*, 736, 104
- Kauffmann, G. et al. 2003, *MNRAS*, 346, 1055
- Kewley, L. J., & Ellison, S. L. 2008, *ApJ*, 681, 1183
- Kobulnicky, H. A., & Kewley, L. J. 2004, *ApJ*, 617, 240
- Kong, X., & Cheng, F. Z. 2002, *A&A*, 389, 845
- Kong, X. 2004, *A&A*, 425, 417
- Kriek, M., van Dokkum, P. G., Labbé, I., et al. 2009, *ApJ*, 700, 221
- Kroupa, P. 2001, *MNRAS*, 322, 231
- Kunth, D., & Östlin, G. 2000, *A&ARv*, 10, 1
- Lara-López, M. A. et al. 2010, *A&A*, 521, L53
- Lee, H., Skillman, E. D., Cannon, J. M., et al. 2006, *ApJ*, 647, 970
- Leitherer, C., Schaerer, D., Goldader, J. D., et al. 1999, *ApJS*, 123, 3
- Lian, J. H., Li, J. R., Yan, W., & Kong, X. 2015, *MNRAS*, 446, 1449
- Lilly, S. J., Le Brun, V., Maier, C., et al. 2009, *ApJS*, 184, 218
- Ly, C., Malkan, M. A., Nagao, T., et al. 2014, *ApJ*, 780, 122
- Maiolino, R. et al. 2008, *A&A*, 488, 463

- Mannucci, F., Cresci, G., Maiolino, R., Marconi, A., & Gnerucci, A. 2010, *MNRAS*, 408, 2115
- Markwardt, C. B. 2009, in *ASP Conf. Ser.*, ed. D. A. Bohlender, D. Durand, & P. Dowler, 411, 251
- Martin, C. L., Shapley, A. E., Coil, A. L., et al. 2012, *ApJ*, 760, 127
- Muzzin, A., Marchesini, D., Stefanon, M., et al. 2013, *ApJS*, 206, 8
- Pettini, M., & Pagel, B. E. J. 2004, *MNRAS*, 348, L59
- Sánchez Almeida, J., Muñoz-Tuñón, C., Amorín, R., et al. 2008, *ApJ*, 685, 194
- Sargent, W. L. W., & Searle, L. 1970, *ApJL*, 162, L155
- Savaglio, S. et al. 2005, *ApJ*, 635, 260
- Shi, F., Kong, X., Li, C., & Cheng, F. Z. 2005, *A&A*, 437, 849
- Lequeux, J., Peimbert, M., Rayo, J. F., Serrano, A., & Torres-Peimbert, S. 1979, *A&A*, 80, 155
- Thuan, T. X., & Martin, G. E. 1981, *ApJ*, 247, 823
- Tremonti, C. A. et al. 2004, *ApJ*, 613, 898
- Yuan, T.-T., Kewley, L. J., & Richard, J. 2013, *ApJ*, 763, 9
- Zahid, H. J., Kewley, L. J., & Bresolin, F. 2011, *ApJ*, 730, 137
- Zhao, Y., Gao, Y., & Gu, Q. 2010, *ApJ*, 710, 663

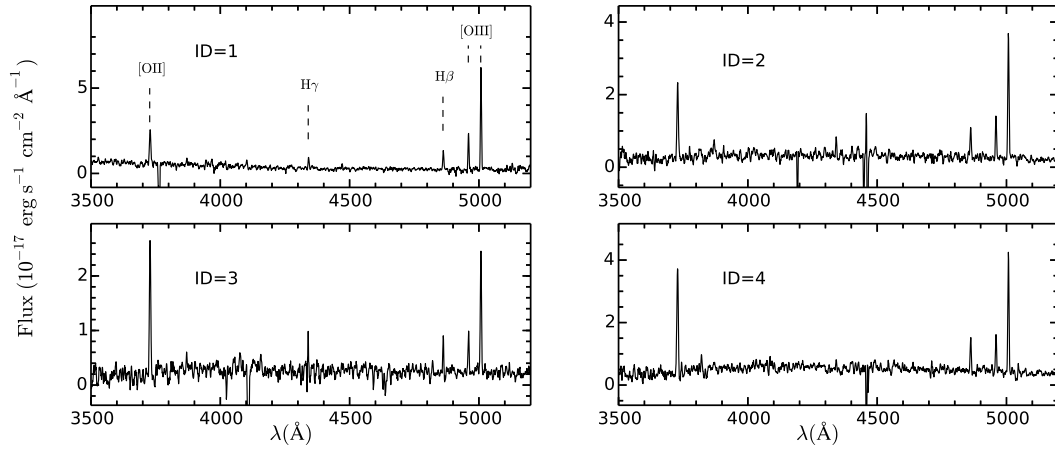


Fig. 1.— Hectospec spectra smoothed using a boxcar of five pixels for the first four COSMOS BCDs as listed in Table 1. Each panel is marked with the corresponding object ID.

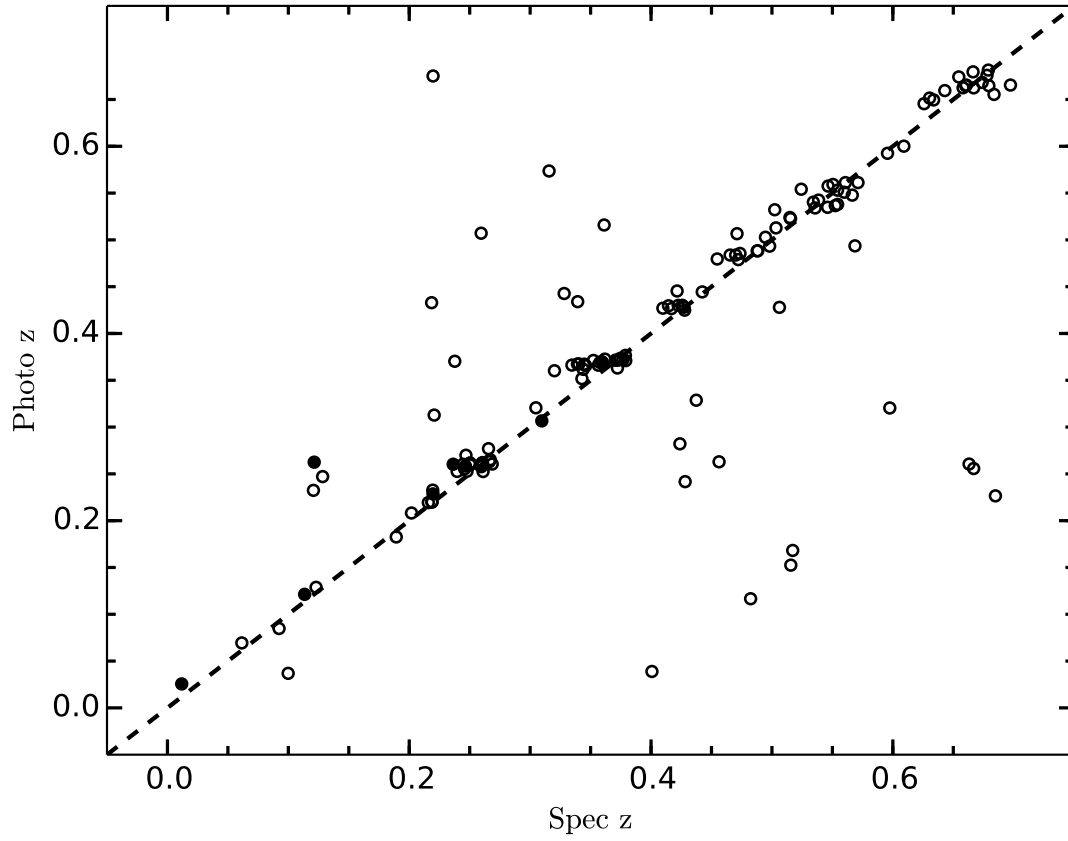


Fig. 2.— Comparison between spectroscopic and photometric redshift for COSMOS BCDs. Filled circles are BCDs with spectroscopic redshift from Lilly et al. (2009). Dashed line indicates equality between the x- and y-axis values.

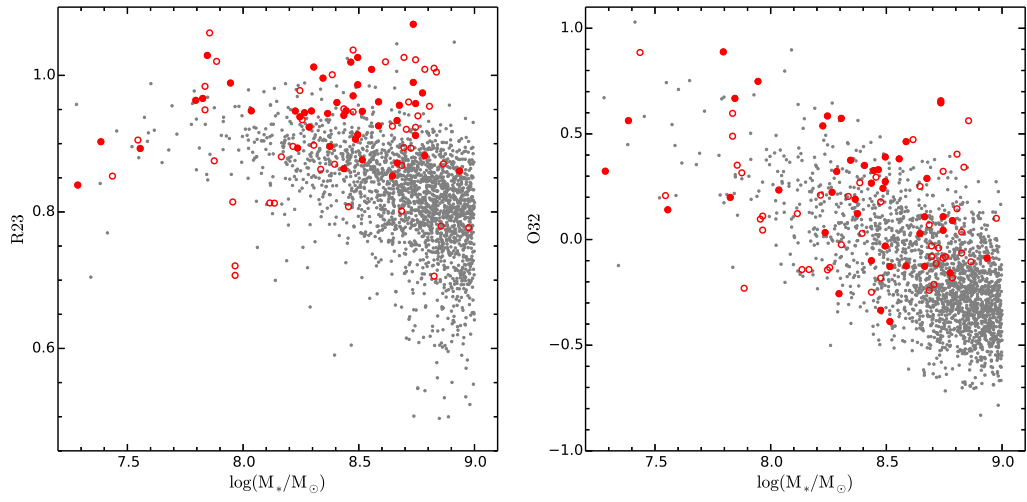


Fig. 3.— R23 ratio (left panel) and O32 ratio (right panel) distribution versus the stellar mass. Grey dots are the SDSS BCDs and red circles are the COSMOS BCDs. The filled circles represent COSMOS BCDs with dust attenuation corrected using the Balmer decrement method.

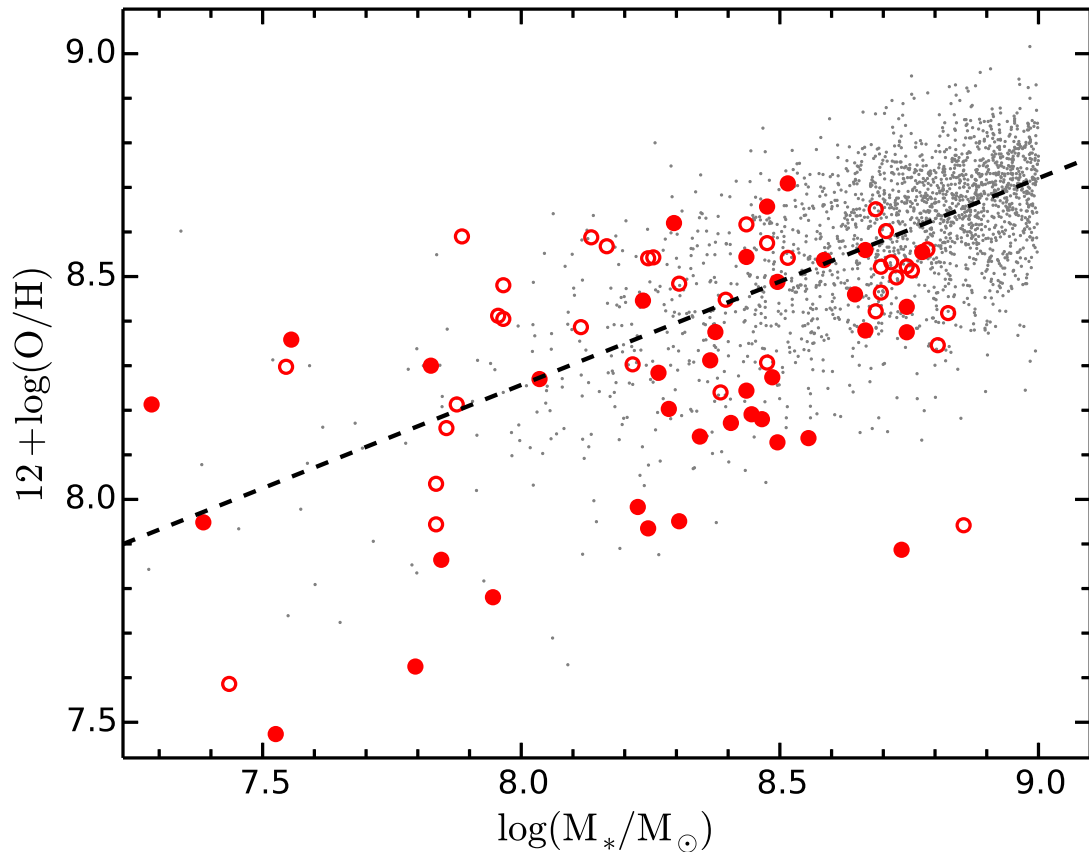


Fig. 4.— Mass-metallicity relation for BCDs. The symbols are the same as Figure 3.

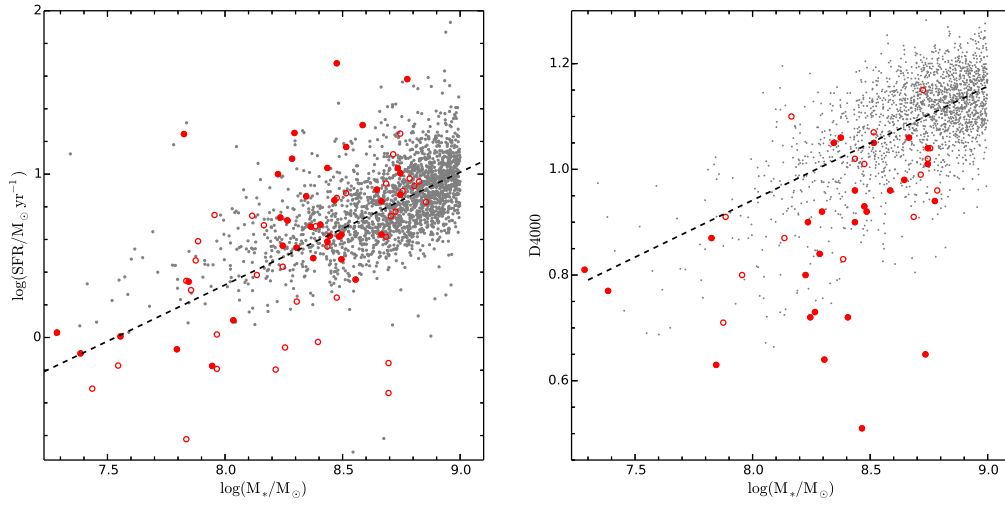


Fig. 5.— Stellar mass versus SFR and $D_n(4000)$ diagram for BCDs. Symbols are the same as Figure 3.

Table 1. Emission line measurements of COSMOS BCD sample.

ID	RA (J2000) h:m:s	Dec (J2000) d:m:s	[O II] λ 3727 ^a	H γ	H β	EW(H β) Å	[O III] λ 4959	[O III] λ 5007
1	09:59:37.39	+02:05:04.8	142.3 \pm 4.0	39.4 \pm 2.0	65.8 \pm 2.0	24.2	110.9 \pm 2.3	298.9 \pm 2.7
2	09:59:15.82	+02:15:27.3	155.8 \pm 6.4	33.7 \pm 3.8	54.6 \pm 3.2	17.5	66.7 \pm 2.8	206.7 \pm 3.8
3	09:59:45.49	+02:08:28.6	285.1 \pm 4.5	-	51.9 \pm 2.1	12.4	57.1 \pm 2.0	187.8 \pm 2.4
4	09:59:27.85	+02:16:04.3	273.0 \pm 6.4	-	75.6 \pm 3.1	12.6	69.5 \pm 2.6	248.7 \pm 3.8
5	09:59:19.76	+02:03:39.9	56.4 \pm 4.6	-	37.7 \pm 2.1	243.7	83.6 \pm 2.4	223.1 \pm 2.8
6	09:58:32.84	+02:26:18.8	121.3 \pm 4.3	29.6 \pm 3.1	52.0 \pm 1.9	17.5	106.2 \pm 2.0	287.9 \pm 3.5
7	09:59:31.40	+02:33:52.7	113.3 \pm 4.5	-	25.3 \pm 2.2	7.4	26.6 \pm 1.8	84.5 \pm 2.2
8	09:59:09.46	+02:25:04.8	200.4 \pm 5.2	-	56.6 \pm 2.6	8.5	114.6 \pm 2.8	302.0 \pm 3.2
9	09:59:15.11	+02:36:33.8	227.7 \pm 4.1	73.2 \pm 2.3	133.8 \pm 2.6	42.0	352.9 \pm 2.9	1010.0 \pm 4.1
10	09:59:08.21	+02:26:00.9	94.7 \pm 5.0	-	29.1 \pm 2.9	13.0	25.9 \pm 2.2	68.3 \pm 2.7
11	10:00:06.00	+02:34:53.7	135.6 \pm 5.4	-	26.2 \pm 2.7	8.2	21.9 \pm 2.5	76.4 \pm 2.6
12	09:58:49.57	+02:04:56.9	188.9 \pm 6.6	77.8 \pm 4.5	138.6 \pm 3.7	104.5	229.4 \pm 4.1	689.9 \pm 4.8
13	09:59:56.98	+02:12:54.9	91.7 \pm 5.0	-	44.4 \pm 3.9	48.3	40.0 \pm 2.8	101.6 \pm 2.8
14	09:59:37.69	+02:09:02.9	35.2 \pm 4.2	-	56.7 \pm 4.0	85.8	98.7 \pm 3.4	270.0 \pm 4.4
15	10:00:05.64	+02:16:08.0	4055.4 \pm 8.1	390.5 \pm 3.7	835.9 \pm 4.1	18.9	1002.0 \pm 4.0	2820.8 \pm 4.8
16	09:59:37.27	+02:12:46.5	117.2 \pm 5.4	-	34.5 \pm 3.2	22.4	44.3 \pm 3.7	110.9 \pm 3.2
17	09:58:44.54	+02:09:54.3	410.0 \pm 5.9	83.3 \pm 3.8	127.4 \pm 3.1	25.1	144.9 \pm 2.9	442.4 \pm 3.7
18	09:58:59.75	+02:18:49.3	70.6 \pm 3.8	20.2 \pm 3.9	25.4 \pm 2.0	61.7	30.4 \pm 1.8	97.7 \pm 2.9
19	09:59:26.78	+02:18:59.3	427.7 \pm 4.4	61.1 \pm 2.4	127.6 \pm 2.1	58.0	183.9 \pm 2.5	549.0 \pm 3.2
20	09:58:51.38	+02:17:57.1	488.4 \pm 6.7	71.4 \pm 3.5	147.4 \pm 3.4	13.8	175.0 \pm 3.3	540.2 \pm 4.4
21	09:59:54.00	+02:18:59.5	153.3 \pm 4.3	34.1 \pm 4.4	65.3 \pm 2.3	39.5	100.8 \pm 3.4	325.3 \pm 3.4
22	09:59:26.41	+02:22:01.7	147.2 \pm 4.3	-	51.3 \pm 2.0	52.5	114.1 \pm 2.1	330.9 \pm 2.5
23	09:58:31.33	+02:23:13.0	299.6 \pm 5.1	57.5 \pm 2.8	118.6 \pm 2.1	60.8	182.6 \pm 2.3	554.0 \pm 3.1
24	09:59:45.54	+02:25:39.6	108.9 \pm 4.4	68.2 \pm 3.0	134.0 \pm 2.7	273.8	281.3 \pm 3.0	841.6 \pm 4.1

Table 1—Continued

ID	RA (J2000) h:m:s	Dec (J2000) d:m:s	[O II] λ 3727 ^a	H γ	H β	EW(H β) Å	[O III] λ 4959	[O III] λ 5007
25	09:59:06.68	+02:26:45.4	76.0 \pm 3.9	-	17.0 \pm 1.9	15.4	30.7 \pm 2.5	54.6 \pm 2.9
26	09:59:30.22	+02:27:21.4	30.9 \pm 3.6	-	18.2 \pm 1.9	18.9	36.0 \pm 2.2	95.2 \pm 2.3
27	09:58:53.41	+02:28:10.1	96.1 \pm 5.5	16.6 \pm 2.7	35.4 \pm 3.3	29.8	53.3 \pm 2.9	165.0 \pm 3.3
28	09:59:07.98	+02:27:51.3	627.9 \pm 6.2	108.0 \pm 3.6	231.0 \pm 3.4	47.3	358.2 \pm 3.4	1051.0 \pm 4.7
29	10:00:03.02	+02:22:21.4	165.5 \pm 3.9	-	35.3 \pm 1.8	45.6	37.8 \pm 2.0	108.7 \pm 1.9
30	09:59:18.10	+02:34:33.3	242.3 \pm 4.1	-	52.3 \pm 2.1	19.2	44.8 \pm 1.9	148.7 \pm 2.2
31	09:59:09.61	+02:35:47.6	157.2 \pm 3.5	-	37.8 \pm 1.6	203.3	8.1 \pm 1.4	130.6 \pm 2.1
32	09:59:56.51	+02:26:25.5	117.4 \pm 3.5	28.9 \pm 2.5	48.7 \pm 1.9	73.3	97.0 \pm 2.2	282.9 \pm 2.7
33	09:59:34.95	+02:27:56.2	55.6 \pm 4.3	-	29.7 \pm 3.2	43.9	23.9 \pm 2.3	71.8 \pm 3.0
34	09:59:40.86	+02:28:47.1	104.8 \pm 4.7	-	24.1 \pm 2.5	27.1	25.3 \pm 2.6	77.2 \pm 3.2
35	09:59:49.14	+02:37:00.1	213.2 \pm 5.3	64.2 \pm 3.5	123.0 \pm 2.5	66.6	253.1 \pm 2.7	798.7 \pm 4.0
36	09:59:21.32	+02:38:54.4	287.9 \pm 6.2	-	69.5 \pm 3.1	10.2	80.1 \pm 3.2	238.6 \pm 3.5
37	09:59:25.29	+02:39:16.3	132.8 \pm 5.5	-	44.4 \pm 2.9	50.0	54.1 \pm 3.3	142.1 \pm 5.4
38	09:59:58.87	+02:29:47.6	330.2 \pm 4.5	55.2 \pm 3.0	106.0 \pm 2.2	63.8	156.3 \pm 2.6	423.4 \pm 3.1
39	09:59:26.96	+02:46:05.4	276.6 \pm 3.6	47.8 \pm 2.2	102.4 \pm 2.1	50.8	201.9 \pm 2.2	592.3 \pm 2.7
40	10:00:01.03	+02:47:35.7	203.3 \pm 6.6	68.2 \pm 3.7	113.6 \pm 3.9	76.4	153.3 \pm 3.6	428.3 \pm 4.1
41	10:00:24.36	+02:27:14.9	195.2 \pm 4.0	37.1 \pm 3.2	66.6 \pm 2.8	26.7	70.5 \pm 2.0	208.3 \pm 2.6
42	10:00:28.57	+02:33:53.2	151.8 \pm 5.3	31.9 \pm 3.1	42.5 \pm 3.0	16.0	55.0 \pm 2.8	141.4 \pm 2.9
43	10:01:05.02	+02:41:04.9	1615.9 \pm 6.3	148.2 \pm 3.7	317.1 \pm 4.2	12.9	301.2 \pm 3.4	895.7 \pm 4.0
44	10:01:23.48	+02:38:11.6	391.0 \pm 5.0	-	97.6 \pm 2.2	12.6	109.2 \pm 2.4	319.3 \pm 2.8
45	10:00:51.99	+02:26:20.8	167.9 \pm 4.2	-	46.9 \pm 2.6	11.0	32.4 \pm 1.9	96.5 \pm 2.1
46	10:01:46.06	+02:36:47.6	979.2 \pm 5.7	94.6 \pm 2.9	202.4 \pm 2.9	13.0	141.5 \pm 2.7	400.9 \pm 3.3
47	10:01:35.13	+02:30:54.9	1893.1 \pm 7.6	194.2 \pm 4.2	415.6 \pm 4.2	15.1	489.0 \pm 3.7	1419.8 \pm 4.6
48	10:01:32.79	+02:30:01.9	158.1 \pm 5.9	59.5 \pm 3.5	106.5 \pm 3.8	35.1	244.5 \pm 3.6	736.5 \pm 4.7

Table 1—Continued

ID	RA (J2000) h:m:s	Dec (J2000) d:m:s	[O II] λ 3727 ^a	H γ	H β	EW(H β) Å	[O III] λ 4959	[O III] λ 5007
49	10:02:08.14	+02:32:13.8	200.4±3.7	48.2±2.4	89.7±2.0	37.9	169.0±1.9	449.5±2.5
50	10:02:05.01	+02:26:44.3	55.2±3.0	-	27.3±2.2	30.5	35.0±2.1	114.2±2.1
51	10:01:57.48	+02:24:20.2	123.9±3.8	-	42.0±1.8	29.2	67.2±1.9	230.0±2.4
52	10:01:30.91	+02:23:02.8	213.3±3.6	58.9±3.8	74.5±2.0	39.0	110.3±2.0	331.1±2.8
53	10:01:10.73	+02:20:49.2	1455.2±9.4	444.9±5.1	924.1±5.3	88.6	1717.4±6.3	5022.1±9.7
54	10:02:14.82	+02:19:36.0	94.9±3.7	-	40.8±1.9	22.7	44.7±2.1	126.0±2.0
55	10:01:52.70	+02:14:15.9	75.0±6.2	95.7±4.2	160.7±3.7	91.1	438.7±4.0	1239.3±5.3
56	10:00:53.37	+02:17:49.2	96.6±3.6	24.3±2.3	42.6±1.9	43.7	78.6±2.4	237.7±2.6
57	10:01:34.72	+02:13:30.3	271.5±4.3	-	58.4±2.0	10.8	53.2±2.2	209.0±3.9
58	10:01:41.88	+02:06:25.1	159.8±5.1	-	37.6±2.0	17.5	51.8±2.1	173.4±4.2
59	10:00:57.40	+02:09:05.8	73.6±3.9	-	29.7±2.0	101.2	40.9±1.9	119.4±2.2
60	10:01:15.57	+02:04:00.3	309.8±5.7	40.4±4.2	83.0±3.2	19.5	76.2±2.8	231.5±3.1
61	10:00:42.57	+02:12:20.4	90.7±5.7	37.0±3.2	78.9±3.4	109.4	169.7±3.5	508.2±4.2
62	10:01:20.81	+01:54:51.5	156.6±3.8	-	54.0±1.9	32.2	58.2±2.0	183.7±2.8
63	10:00:46.26	+01:55:48.5	296.2±4.0	-	93.7±2.2	41.2	133.7±2.1	414.2±2.7
64	10:00:18.29	+02:03:11.8	121.8±4.3	-	26.3±1.8	147.8	43.6±2.7	113.6±2.3
65	10:00:28.31	+02:01:24.7	3586.7±5.4	295.3±3.4	632.1±2.3	30.4	653.2±2.4	1659.3±2.9
66	09:59:41.99	+01:58:17.7	183.5±4.8	36.0±3.2	77.0±2.2	36.8	116.7±2.3	320.7±2.6
67	10:00:06.45	+02:09:14.0	220.8±5.4	78.6±3.3	156.3±2.6	71.8	290.3±3.0	848.5±4.0
68	09:59:28.49	+01:56:47.7	333.5±6.0	-	84.7±3.2	15.2	69.7±3.0	240.6±3.1
69	10:02:08.43	+02:27:21.4	59.3±2.9	-	60.0±1.9	35.6	84.9±2.0	216.5±2.6
70	10:01:12.67	+02:34:14.8	854.3±5.5	111.0±3.2	237.5±2.9	23.2	200.8±2.6	678.9±3.8
71	10:01:46.92	+02:41:50.9	496.1±5.1	87.8±2.8	167.9±2.4	28.0	272.4±3.2	785.2±3.9
72	10:01:50.75	+02:26:49.8	243.9±4.1	-	41.3±1.8	26.6	46.0±2.0	143.4±2.3

Table 1—Continued

ID	RA (J2000) h:m:s	Dec (J2000) d:m:s	[O II] λ 3727 ^a	H γ	H β	EW(H β) Å	[O III] λ 4959	[O III] λ 5007
73	09:59:57.35	+01:52:17.9	57.7 \pm 3.6	-	24.0 \pm 1.8	14.7	26.6 \pm 1.9	72.0 \pm 2.0
74	10:00:35.77	+02:16:33.3	72.9 \pm 5.6	-	27.7 \pm 3.9	30.0	31.8 \pm 2.3	117.7 \pm 3.3

^aAll the emission lines have units of 10^{-18} erg s $^{-1}$ cm $^{-2}$ and EW of Å.

Table 2. Physical properties of COSMOS BCD sample.

ID	z	A_V ^a mag	$\log M_*$ M_\odot	$12+\log(\text{O}/\text{H})$	$\log(\text{SFR})$ ^b $M_\odot \text{ yr}^{-1}$	$D_n(4000)$
1	0.482	0.0	8.29	8.20±0.04	0.88±0.03	0.8
2	0.250	0.0	8.38	8.38±0.06	0.16±0.01	1.1
3	0.358	(0.4)	8.79	8.56±0.03	0.34±0.01	1.0
4	0.250	(0.1)	8.73	8.50±0.03	0.22±0.01	1.1
5	0.305	(0.0)	7.84	7.94±0.13	0.17±0.01	-
6	0.372	0.0	8.35	8.14±0.06	0.37±0.01	1.1
7	0.356	(0.0)	8.52	8.54±0.06	0.17±0.01	1.1
8	0.261	(0.2)	8.48	8.31±0.04	0.18±0.01	1.0
9	0.427	0.0	8.74	7.89±0.03	1.34±0.03	0.7
10	0.261	(0.0)	8.14	8.59±0.08	0.09±0.01	0.9
11	0.266	(0.1)	8.44	8.62±0.06	0.09±0.01	1.0
12	0.202	0.0	7.39	7.95±0.06	0.24±0.01	0.8
13	0.267	(0.0)	7.97	8.48±0.09	0.15±0.01	-
14	0.221	(0.0)	7.44	7.59±0.18	0.12±0.01	-
15	0.236	1.4	8.78	8.55±0.00	2.11±0.01	0.9
16	0.261	(0.0)	8.31	8.48±0.07	0.11±0.01	0.7
17	0.260	0.0	8.24	8.45±0.02	0.40±0.01	0.9
18	0.372	0.0	7.56	8.36±0.08	0.18±0.01	-
19	0.426	0.0	8.75	8.38±0.01	1.27±0.02	1.0
20	0.246	0.0	8.75	8.43±0.02	0.41±0.01	1.0
21	0.377	0.0	8.45	8.19±0.04	0.49±0.02	-
22	0.340	(0.4)	7.86	8.16±0.04	0.30±0.01	-
23	0.339	0.0	8.44	8.24±0.02	0.69±0.01	0.9
24	0.320	0.0	7.80	7.62±0.06	0.68±0.01	-

Table 2—Continued

ID	z	A_V^a mag	$\log M_*$ M_\odot	$12+\log(\text{O}/\text{H})$	$\log(\text{SFR})^b$ $M_\odot \text{ yr}^{-1}$	$D_n(4000)$
25	0.372	(0.1)	8.25	8.54 ± 0.08	0.12 ± 0.01	-
26	0.362	(0.0)	7.84	8.04 ± 0.19	0.12 ± 0.01	-
27	0.260	0.3	8.04	8.27 ± 0.08	0.11 ± 0.01	0.8
28	0.260	0.4	8.27	8.28 ± 0.01	0.72 ± 0.01	0.7
29	0.359	(0.3)	8.48	8.57 ± 0.04	0.23 ± 0.01	-
30	0.343	(0.1)	8.71	8.60 ± 0.03	0.31 ± 0.01	1.0
31	0.444	(0.1)	8.70	8.52 ± 0.03	0.42 ± 0.02	-
32	0.426	0.0	8.56	8.14 ± 0.04	0.49 ± 0.02	-
33	0.247	(0.0)	7.97	8.40 ± 0.13	0.08 ± 0.01	-
34	0.250	(0.0)	8.26	8.54 ± 0.07	0.07 ± 0.01	-
35	0.335	0.0	8.31	7.95 ± 0.04	0.69 ± 0.01	0.6
36	0.269	(0.1)	8.76	8.51 ± 0.03	0.24 ± 0.01	1.0
37	0.259	(0.1)	8.40	8.45 ± 0.07	0.14 ± 0.01	-
38	0.379	0.0	8.67	8.38 ± 0.02	0.80 ± 0.02	-
39	0.428	0.5	8.47	8.18 ± 0.02	1.03 ± 0.02	0.5
40	0.219	0.0	7.29	8.21 ± 0.05	0.24 ± 0.01	0.8
41	0.417	0.0	8.65	8.46 ± 0.03	0.63 ± 0.03	1.0
42	0.266	0.0	8.50	8.49 ± 0.05	0.14 ± 0.01	-
43	0.220	1.4	8.30	8.62 ± 0.01	0.68 ± 0.01	0.9
44	0.360	(0.1)	8.75	8.52 ± 0.02	0.65 ± 0.01	1.0
45	0.344	(0.2)	8.69	8.65 ± 0.04	0.28 ± 0.02	0.9
46	0.246	0.8	8.52	8.71 ± 0.01	0.56 ± 0.01	1.1
47	0.219	0.9	8.59	8.54 ± 0.01	0.89 ± 0.01	1.0
48	0.219	0.0	7.85	7.86 ± 0.06	0.23 ± 0.01	0.6

Table 2—Continued

ID	z	A_V ^a mag	$\log M_*$ M_\odot	$12+\log(\text{O}/\text{H})$	$\log(\text{SFR})$ ^b $M_\odot \text{ yr}^{-1}$	$D_n(4000)$
49	0.346	0.0	8.41	8.17±0.03	0.55±0.01	0.7
50	0.422	(0.0)	7.88	8.21±0.09	0.26±0.02	0.7
51	0.422	(0.1)	8.39	8.24±0.04	0.41±0.02	0.8
52	0.375	0.0	8.37	8.31±0.02	0.55±0.01	-
53	0.248	0.0	8.23	7.98±0.01	2.60±0.01	0.8
54	0.410	(0.4)	8.12	8.39±0.06	0.37±0.02	-
55	0.216	0.0	7.53	7.47±0.06	0.33±0.01	0.6
56	0.474	0.0	8.50	8.13±0.06	0.55±0.02	-
57	0.371	(0.3)	8.72	8.53±0.03	0.42±0.01	1.0
58	0.465	(0.3)	8.83	8.42±0.05	0.46±0.02	-
59	0.352	(0.0)	8.22	8.30±0.08	0.19±0.01	-
60	0.310	0.0	8.67	8.56±0.03	0.39±0.02	1.1
61	0.244	0.0	7.95	7.78±0.10	0.21±0.01	-
62	0.373	(0.0)	8.69	8.42±0.04	0.39±0.01	-
63	0.442	(0.3)	8.81	8.35±0.02	1.02±0.02	-
64	0.379	(0.2)	8.70	8.46±0.05	0.20±0.01	-
65	0.361	1.7	8.48	8.66±0.00	4.25±0.02	0.9
66	0.339	0.4	8.49	8.27±0.04	0.45±0.01	0.9
67	0.316	0.0	8.25	7.93±0.04	0.77±0.01	0.7
68	0.238	(0.2)	8.17	8.57±0.03	0.22±0.01	1.1
69	0.456	(0.1)	8.86	7.94±0.11	0.70±0.02	0.5
70	0.259	1.0	8.44	8.54±0.01	0.74±0.01	1.0
71	0.401	0.0	7.83	8.30±0.01	1.45±0.02	0.9
72	0.375	(0.4)	7.89	8.59±0.03	0.30±0.01	0.9

Table 2—Continued

ID	z	A_V ^a mag	$\log M_*$ M_\odot	$12+\log(\text{O}/\text{H})$	$\log(\text{SFR})$ ^b $M_\odot \text{ yr}^{-1}$	$D_n(4000)$
73	0.428	(0.0)	7.96	8.41 ± 0.09	0.24 ± 0.02	0.8
74	0.220	(0.0)	7.55	8.30 ± 0.12	0.06 ± 0.01	-

^aThe dust attenuation A_V from SED fitting is listed within parantheses.

^bThe listed SFR are not corrected for burst age which can be done by comining the $\text{EW}(\text{H}\beta)$ listed in Table 1 and equation (5) in Izotov et al. (2015).